spin it down extremely efficiently at the very beginning of the evolution. This is related to the small (because it is proportional to r^2) amount of angular momentum in the core. Once the core has been spun down, the damping of retrograde waves, which carry the negative angular momentum, increases locally. Consequently, a "slowliness" front forms and propagates in a wave-like way from the core to the surface. As further braking proceeds, a second front forms and propagates outward. The time scale for angular momentum extraction through differential wave filtering in a Sun-like star is of the order of a few 10^7 years (*8*, *9*). It adjusts itself so as to compensate for the flux of angular momentum that is lost through the stellar wind. This explains why front propagation is fast at the beginning and then slows down, just as the spin-down rate does.

Figure 2 shows the predicted evolution of the surface lithium abundance together with the data for solar mass stars in open clusters of various ages. In the case without IGWs, lithium depletion is always too strong. However, thanks to IGWs, the transport of elements and the resulting lithium depletion are considerably reduced because of the flattening of the internal rotation profile. Our calculations with IGWs fit the data quite well. The smallness of the observed dispersion in the lithium content is well explained even with a realistic and thus large range for the initial rotation velocity. This process is also self-regulating, and as such, our results do not depend qualitatively on the total wave flux used as long as it is large enough (that is, ~0.01% of the convective energy).

The presence of a dynamo magnetic field at the convective interface (termed a tachocline) would not qualitatively change the results presented here. A strong magnetic field (10^5 G) may prevent very low frequency waves ($\omega < 0.1$ μHz for $l = 2$, where ω is frequency and l is spherical harmonic degree) from propagating (*14*, *23*). The lowest frequency used for the calculations presented here is $\omega = 0.5$ μHz. The low-degree waves that deposit angular momentum in the interior are thus not affected. Although the disappearance of high-degree, low-frequency waves could affect SLO dynamics, this has a negligible impact on filtering (*15*), which is dominated by the velocity difference on both sides of the SLO.

These results show in principle the ability of IGWs to efficiently extract angular momentum from the deep interior of solar-type stars on a very short time scale and as such, nullify the argument made by Gough and McIntyre (*24*) about the "inevitability of a magnetic field" in the solar interior. Our hydrodynamic model, which uses the same free parameters to describe rotational mixing as those that successfully reproduce abundance anomalies in massive stars (*5*), successfully shapes both the rotation profile and the time evolution of the surface lithium abundance in these objects. In order to compare it to other models that rely on a fossil magnetic field (*25*), better helioseismic constraints are needed. The presence of a negative rotation gradient, for example, would strongly point toward wave transport. Our comprehensive picture should have implications for other difficult unsolved problems related to the transport of chemicals and angular momentum in low-mass stars. We think in particular of halo dwarf stars and the related cosmological problem of the primordial lithium and of giants on the horizontal and asymptotic giant branches that exhibit unexplained abundance anomalies.

References and Notes

1. W. J. Chaplin *et al.*, *Mon. Not. R. Astron. Soc.* **308**, 405 (1999).
2. S. Couvidat *et al.*, *Astrophys. J.* **597**, L77 (2003).
3. B. Chaboyer, P. Demarque, M. H. Pinsonneault, *Astrophys. J.* **441**, 865 (1995).
4. J. Matias, J.-P. Zahn, in *Sounding Solar and Stellar Interiors*, J. Provost, F.-X. Schmider, Eds. (IAU Symposium 181, Observatoire de la Côte d'Azur, Nice, France, 1998), pp. 103–104.
5. A. Maeder, G. Meynet, *Annu. Rev. Astron. Astrophys.* **38**, 143 (2000).
6. P. Charbonneau, K. B. MacGregor, *Astrophys. J.* **417**, 762 (1993).
7. P. Eggenberger, A. Maeder, G. Meynet, *Astron. Astrophys.* **440**, L9 (2005).
8. J.-P. Zahn, S. Talon, J. Matias, *Astron. Astrophys.* **322**, 320 (1997).
9. P. Kumar, E. Quataert, *Astrophys. J.* **475**, L143 (1997).
10. M. E. McIntyre, in *Perspectives in Fluid Dynamics: A Collective Introduction to Current Research*, G. K. Batchelor, H. K. Moffatt, M. G. Worster, Eds. (Cambridge Univ. Press, Cambridge, 2003), pp. 557–624.
11. M. P. Baldwin *et al.*, *Rev. Geophys.* **39**, 179 (2001).
12. O. Ringot, *Astron. Astrophys.* **335**, L89 (1998).
13. P. Kumar, S. Talon, J.-P. Zahn, *Astrophys. J.* **520**, 859 (1999).
14. S. Talon, P. Kumar, J.-P. Zahn, *Astrophys. J.* **574**, L175 (2002).
15. S. Talon, C. Charbonnel, *Astron. Astrophys., Astron. Astrophys.* **440**, 981 (2005).
16. For shear turbulence, we use a prescription for the turbulent viscosity ν_v and diffusivity D_v by comparing the kinetic energy gained from differential rotation to the cost of moving against a stably stratified background. We get $\nu_v = D_v = 2\,Ri_c\left(\frac{d\Omega}{d\ln r}\right)^2 \frac{K}{g}\frac{dr}{d\ln\theta}$, where the critical Richardson number is assumed to be $Ri_c = 1/4$, Ω is the rotation rate, r is the radial coordinate, K is the thermal diffusivity, g is the gravitational acceleration, and θ is the potential temperature.
17. S. D. Kawaler, *Astrophys. J.* **333**, 236 (1988).
18. Y. Gaigé, *Astron. Astrophys.* **269**, 267 (1993).
19. P. Goldreich, N. Murray, P. Kumar, *Astrophys. J.* **424**, 466 (1994).
20. Wave excitation is proportional to the convective energy flux ρv^3 as well as to a function of the radial and horizontal amplitudes (ξ_r and ξ_h, respectively) of the evanescent wave in the convective region and is given by $F_E(l,\omega) = \frac{\omega^2}{4\pi}\int_{r_c}^{R} dr\,\rho^2 r^2\left[\left(\frac{\partial\xi_r}{\partial r}\right)^2 + l(l+1)\left(\frac{\partial\xi_h}{\partial r}\right)^2\right]\exp\left[\frac{-h_\omega^2 l(l+1)}{2r^2}\right]\frac{v^3\,L^4}{1+(\omega\tau_L)^{15/2}}$, where R is the radius at the top of the convection zone, r_c is the radius at the bottom, h_ω is the radial size of the largest eddy with frequency ω, L is the size of an energy-bearing eddy, and $\tau_L \approx L/v$ is the convective time.
21. N. E. Hurlburt, J. Toomre, J. M. Massaguer, *Astrophys. J.* **311**, 563 (1986).
22. B. Dintrans, A. Brandenburg, A. Nordlund, R. F. Stein, *Astron. Astrophys.* **438**, 365 (2005).
23. G. Barnes, K. B. MacGregor, P. Charbonneau, *Astrophys. J.* **498**, L169 (1998).
24. D. Gough, M. E. McIntyre, *Nature* **394**, 755 (1998).
25. G. Barnes, P. Charbonneau, K. B. MacGregor, *Astrophys. J.* **511**, 466 (1999).
26. S. Balachandran, *Astrophys. J.* **446**, 203 (1995).
27. B. F. Jones, D. Fischer, D. R. Soderblom, *Astron. J.* **117**, 330 (1999).
28. L. Pasquini *et al.*, *Astron. Astrophys.* **424**, 951 (2004).
29. S. Randich, L. Pasquini, R. Pallavicini, *Astron. Astrophys.* **356**, L25 (2000).
30. P. Sestito, S. Randich, R. Pallavicini, *Astron. Astrophys.* **426**, 809 (2000).
31. D. R. Soderblom, S. B. Fedele, B. F. Jones, J. R. Stauffer, C. F. Prosser, *Astron. J.* **106**, 1080 (1993).
32. J. A. Thorburn, L. M. Hobbs, C. P. Deliyannis, M. H. Pinsonneault, *Astrophys. J.* **415**, 150 (1993).

33. We thank J.-O. Goussard, M. Grenon, G. Meynet, D. Pfenniger, and D. Schaerer, as well as anonymous referees and our editor for suggestions that improved the clarity of this text. Supported by the Natural Sciences and Engineering Research Council of Canada (S.T.).

1 July 2005; accepted 30 August 2005
10.1126/science.1116849

Imaging Spin Transport in Lateral Ferromagnet/ Semiconductor Structures

S. A. Crooker,[1]* M. Furis,[1] X. Lou,[2] C. Adelmann,[3] D. L. Smith,[4] C. J. Palmstrøm,[3] P. A. Crowell[2]

We directly imaged electrical spin injection and accumulation in the gallium arsenide channel of lateral spin-transport devices, which have ferromagnetic source and drain tunnel-barrier contacts. The emission of spins from the source was observed, and a region of spin accumulation was imaged near the ferromagnetic drain contact. Both injected and accumulated spins have the same orientation (antiparallel to the contact magnetization), and we show that the accumulated spin polarization flows away from the drain (against the net electron current), indicating that electron spins are polarized by reflection from the ferromagnetic drain contact. The electrical conductance can be modulated by controlling the spin orientation of optically injected electrons flowing through the drain.

Three essential elements of a semiconductor spin transport device are as follows: (i) a mechanism for electrically injecting spin-polarized electrons, (ii) a practical means for spin manipulation and transport, and (iii) an electronic scheme for detecting the resulting spin po-

larization. It was recently demonstrated that ferromagnetic metals provide a source of spin-polarized electrons in devices using Schottky tunnel barriers between transition metal ferromagnets and semiconductors. Steady-state spin polarizations >25% can be maintained in structures with a ferromagnetic metal source and a light-emitting diode spin detector (*1*–*3*). The detected spins in these experiments are confined to the region immediately underneath the injector, but an independent means of manipulating the injected spins, particularly through precessional phenomena (*4*), is realized more easily in a lateral device geometry. Recent experiments have demonstrated coherent precessional phenomena over 100-μm length scales (*5*), strain-induced spin precession of lateral electron flows (*6*, *7*), current-induced spin polarization (*8*), and the spin Hall effect (*9*, *10*), providing motivation for integrating ferromagnetic spin injectors and detectors into lateral semiconductor spin-transport devices. All-metallic prototypes (*11*, *12*) with ferromagnetic contacts have been demonstrated, but experiments on analogous semiconductor devices with ferromagnetic injectors have been less conclusive (*13*–*16*), largely because there has been no demonstration of precessional phenomena in a semiconductor electrical spin-transport measurement.

Here we report the direct observation of spin injection, transport, accumulation, and detection in devices with metallic ferromagnetic source and drain contacts at opposite ends of a lightly-doped (100) *n*-type GaAs (with layers Si-doped for $n = 2 \times 10^{16}$ cm^{-3}) semiconductor channel. Each contact, which can be used as either an injector or detector, is a Schottky tunnel barrier formed by an epitaxial iron (Fe) film grown on a highly doped n^+-GaAs layer (*17*). Scanning Kerr microscopy (*7*, *9*, *18*) was used to image the spin transport in the 300-μm-long channel region. We present data from devices in which the channel is parallel to the [011] direction ($\pm\hat{x}$ direction in Fig. 1A) along the Fe magnetization vector **M**. Similar results were obtained with heterostructures from different growths and with devices having different channel and contact geometries.

The devices were mounted, strain-free, on the vacuum cold finger of an optical cryostat (temperature $T = 4$ K). Uniform uniaxial stress along the [011] GaAs axis could be applied in situ using a cryogenic vise built into the cold finger (*7*). In the *n*-GaAs channel (Fig. 1A), the $\hat{z}$ component of the conduction electron spin polarization (S_z) was measured by detecting the Kerr (light polarization) rotation angle θ_K of a linearly polarized probe laser that was reflected from the sample at normal incidence (*17*). Positive θ_K indicates positive S_z.

Images of the steady-state electron spin polarization S_z in the *n*-GaAs channel near the source and drain contacts (Fig. 1B) at a bias voltage $V_b = +0.4$ V show injection and lateral flow of spin-polarized electrons. These electrons have initial spin **S** along **M** ($\pm\hat{x}$). Without a magnetic field along $\hat{y}$, **S** remains in-plane, yielding $S_z = 0$ and no Kerr rotation θ_K. These images were therefore obtained using a small in-plane magnetic field ($B_y = +3.6$ G), which forces the injected electrons to precess in the *x*-*z* plane. With **M** parallel to $-\hat{x}$ as shown, measuring θ_K ($\propto S_z$) versus B_y (Fig. 1C) confirms that the injected electrons have initial spin **S** that is antiparallel to **M** and therefore parallel to the majority electron spin polarization in Fe. Reversing B_y inverts the direction of spin precession, so that θ_K changes sign. We note that $\theta_K(B_y)$ inverts when **M** is reversed, as expected. By comparison with optical pumping results, we estimate the injected electron spin polarization to be 5 to 10%. No spin precession signal is observed anywhere in a control device with aluminum contacts.

The decay length of the injected spin polarization (~50 μm) is much less than the 300-μm channel length. Therefore, the injected spins lose polarization long before they reach the drain contact. However, the right-hand side of Fig. 1B reveals an appreciable electron spin polarization in the channel within ~10 μm of the drain. The sign of θ_K and the shape of the $\theta_K(B_y)$ curves (Fig. 1D) are the same as for the injected electrons near the source. Therefore, the electron spin polarization that accumulates near the Fe drain contact is also oriented antiparallel to **M** (along $\pm\hat{x}$).

We determined the momentum (**k**) direction of the spin-polarized electrons near the drain by exploiting symmetries of the effective magnetic fields that arise from strain-induced spin-orbit coupling in GaAs. Spin precession of flowing electrons can be observed in strained samples (*6*), and the ef-

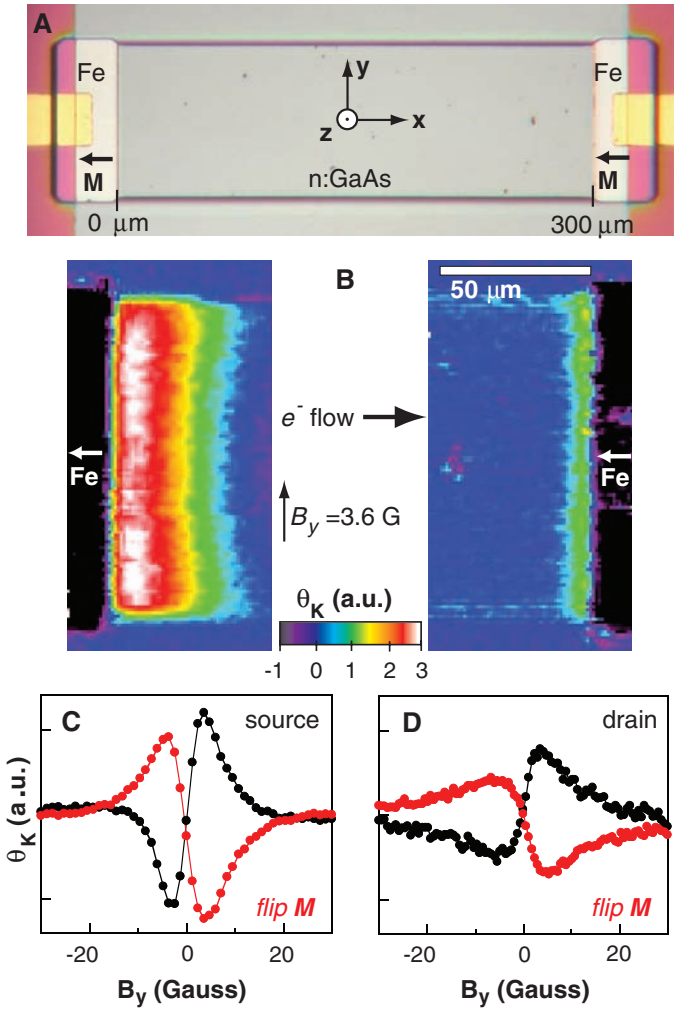

Fig. 1. (**A**) Photomicrograph of the lateral ferromagnet/semiconductor device used for electron spin injection, transport, accumulation, and detection. The Fe/GaAs Schottky tunnel barrier source/drain contacts have [011] easy-axis Fe magnetization **M** along $-\hat{x}$ as shown. The *n*-GaAs channel is 300 μm × 100 μm. (**B**) Images of Kerr rotation angle θ_K ($\propto S_z$) near the source and drain contacts. $V_b = +0.4$ V. The region of spin accumulation near the drain contact also exhibits positive θ_K, indicating that both the injected and accumulated spin polarizations are antiparallel to **M**. (**C**) θ_K versus B_y measured in the *n*-GaAs channel at a point ~10 μm from the source contact, with **M** antiparallel (black) and parallel (red) to $\hat{x}$. $V_b = +0.4$ V. (**D**) Same as (C), but measured at a point 4 μm from the drain contact ($x = 296$ μm). a.u., arbitrary units.

[1]National High Magnetic Field Laboratory, Los Alamos National Laboratory, Los Alamos, NM 87545, USA. [2]School of Physics and Astronomy, University of Minnesota, 116 Church Street SE, Minneapolis, MN 55455, USA. [3]Department of Chemical Engineering and Materials Science, University of Minnesota, 421 Washington Avenue SE, Minneapolis, MN 55455, USA. [4]Theoretical Division, Los Alamos National Laboratory, Los Alamos, NM 87545, USA.

*To whom correspondence should be addressed. E-mail: crooker@lanl.gov

fective fields themselves can be controlled with uniaxial stress along the <011> axes (*7*). The uniaxial stress couples electron spin σ to the off-diagonal elements $\varepsilon_{\alpha\beta}$ of the crystallographic strain tensor. For electrons moving laterally in the *x*-*y* sample plane, the spin-orbit Hamiltonian is $H_S \propto \varepsilon_{\alpha\beta}(\sigma_y k_x - \sigma_x k_y)$ (*19*), which describes an effective magnetic field $\mathbf{B}_\varepsilon$ that is in-plane and orthogonal to **k**. Electrons with **k** parallel to $+\hat{x}$ (Fig. 1A) precess about an effective magnetic field that is parallel to $+\hat{y}$, whereas electrons with momentum –**k** precess in the opposite direction about an effective magnetic field that is parallel to $-\hat{y}$. Thus, $\mathbf{B}_\varepsilon$ either augments or opposes the applied field B_y, shifting the $\theta_K(B_y)$ curves to the right or left depending on the spin flow direction. Small [011] stresses were applied to the device substrate, and $\varepsilon_{\alpha\beta}$ was measured by the GaAs band-edge blue shift (*7*). The resulting effective field $\mathbf{B}_\varepsilon$ (parallel to $\pm\hat{y}$) induces spin precession in the *x*-*z* plane, even when $B_y = 0$ (Fig. 2A). These images also reveal the polarization that accumulates near the drain contact; however, the sign of θ_K is negative—opposite to that of the injected electrons—and in direct contrast with Fig. 1B, which was acquired with a real magnetic field B_y. The $\theta_K(B_y)$ curves measured near the source contact (Fig. 2B) shift to the left with increasing stress ($\mathbf{B}_\varepsilon$ parallel to $+\hat{y}$), whereas curves measured near the drain (Fig. 2C) shift to the right ($\mathbf{B}_\varepsilon$ parallel to $-\hat{y}$). Therefore, the spin-polarized electrons near the source and drain contacts move in opposite directions, indicating that the polarized spins near the drain are traveling along $-\hat{x}$, against the net electron current and away from the drain. These results demonstrate explicitly that electrons near the drain contact become polarized by spin-dependent reflection from the Fe/GaAs tunnel barrier.

Spin polarization by reflection from a ferromagnet/semiconductor interface has been studied theoretically (*20*) and was observed by using optical pumping (*21*, *22*) and in GaAs/MnAs Schottky diodes (*18*) under large forward bias (>1 V). Given the low-resistance tunnel junctions in the present design, spin accumulation is observed at biases down to 50 mV, for which the small drift velocity allows electrons polarized by reflection to diffuse "backstream" into the channel by nearly one spin diffusion length (~10 μm). In all devices and for all device biases $0.050\ \text{V} \le V_b \le 1.0\ \text{V}$, the accumulated (and injected) spin polarization is antiparallel to **M**.

Figure 3A shows $\theta_K(B_y)$ curves acquired in the *n*-GaAs channel, 65 μm from the source contact. In contrast to measurements near the contacts, these data exhibit multiple oscillations. We consider a simple model for spin transport in the channel. Spin-polarized electrons, injected with $S_0 = S_x$ (at $x = 0$ and time $t = 0$) and having a drift velocity v_d, precess as they flow down the channel, arriving at the point of detection x_0 at a later time $t = x_0/v_d$. At this point, $S_z = S_0 \exp(-t/\tau_s)\sin(\Omega_L t)$, where τ_s is the spin lifetime and $\Omega_L = g_e\mu_B B_y/\hbar$ is the Larmor precession frequency, where g_e is the electron *g* factor, μ_B is the Bohr magneton, and $\hbar$ is Planck's constant divided by 2π. The actual signal is therefore computed by averaging the spin orientations of the precessing electrons over the Gaussian distribution of their arrival times (which has a half-width determined by diffusion)

$$S_z(B_y) = \int_{x_0}^{x_0+w}\int_0^\infty \frac{S_0}{\sqrt{4\pi Dt}} e^{-(x - v_d t)^2/4Dt} \times e^{-t/\tau_s}\sin(\Omega_L t)\,dt\,dx \quad (1)$$

where *D* is the diffusion constant, $v_d = \mu E$ is the drift velocity, μ is the electron mobility and *E* is the electric field, and the spatial integral accounts for the width *w* of the source contact (*23*). This type of averaging is the basis of the Hanle effect observed in optical pumping experiments and previous spin-transport experiments in metals (*11*, *12*) and semiconductors (*4*, *8*, *18*, *24*). A calculation of S_z at $x_0 = 65$ μm is shown in Fig. 3A. Good agreement with the data are obtained using $D = 10\ \text{cm}^2/\text{s}$, $v_d = 2.8 \times 10^4$ cm/s, and $\tau_s = 125$ ns. The large drift velocity and spin lifetime in our devices allow access to a spatial regime far from the contacts and well beyond a spin diffusion length ($x_0 > \sqrt{D\tau_s}$), in which the average time of flight from the source to the point of detection, $T = (x_0 + w/2)/v_d$, determines the "age" of the measured spins. In this limit, the first peak in the data ($B_y = B_{peak}$) is the field in which electrons precess through one-quarter Larmor cycle, so that $T = \pi/(2\Omega_L) = \pi\hbar/(2g_e\mu_B B_{peak})$. In Fig. 3A, $x_0 = 65$ μm and $B_{peak} = 1.35$ G, indicating that $T \sim 300$ ns, and $v_d \sim 2.8 \times 10^4$ cm/s.

At a fixed bias, Fig. 3B shows $\theta_K(B_y)$ curves acquired at 16-μm increments from the source contact, demonstrating that injected spins are readily observable up to 120 μm from the source. Further from the source, the average age of the measured spins increases. As a result, B_{peak} decreases, and the amplitude of the signal decreases because of spin relaxation. Figure 3C shows similar data acquired at 2-μm intervals from the drain contact, demonstrating the much shorter length scale for spin accumulation. The evolution of the $\theta_K(B_y)$ curves near both contacts is captured very well by Eq. 1 with a single set of parameters (fig. S2, A and B). Strain effects are modeled using the approach of (*7*), and the results (fig. S2, C and D) show good qualitative agreement with the data of Fig. 2, B and C.

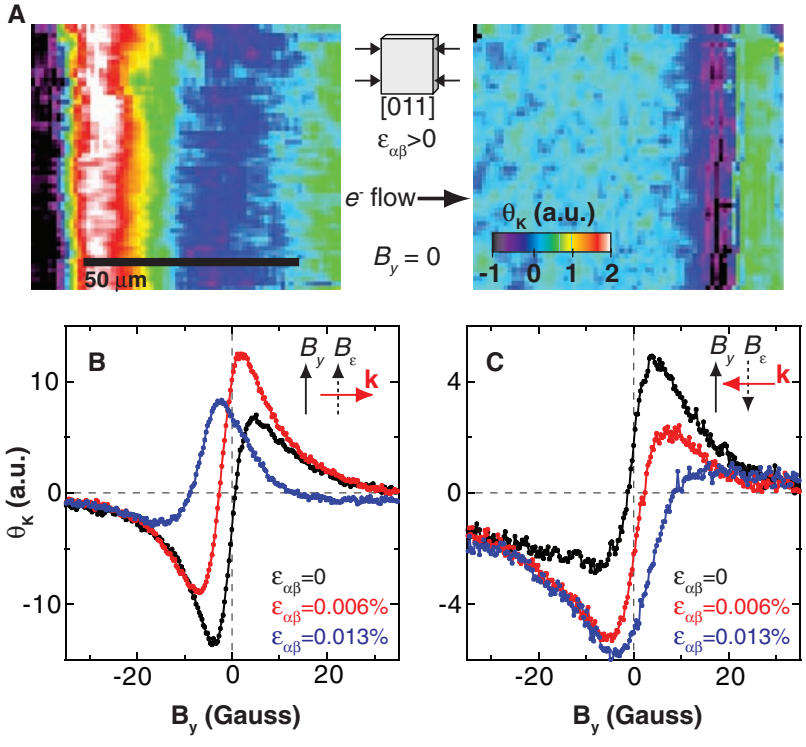

Fig. 2. (**A**) Images of θ_K near the source and drain contacts, in the presence of a small effective magnetic field $\mathbf{B}_\varepsilon$ induced by off-diagonal strain $\varepsilon_{\alpha\beta}$ (due to applied [011] uniaxial stress). $B_y = 0$ and $V_b = +0.4$ V. (**B** and **C**) $\theta_K(B_y)$ curves acquired at points 4 μm from (**B**) the source and (**C**) the drain contact, for three values of uniaxial stress. Curves shift to the left at the source contact and shift to the right at the drain contact, indicating that the spin-polarized electrons accumulated near the drain contact are flowing away from the drain (against the net electron current).

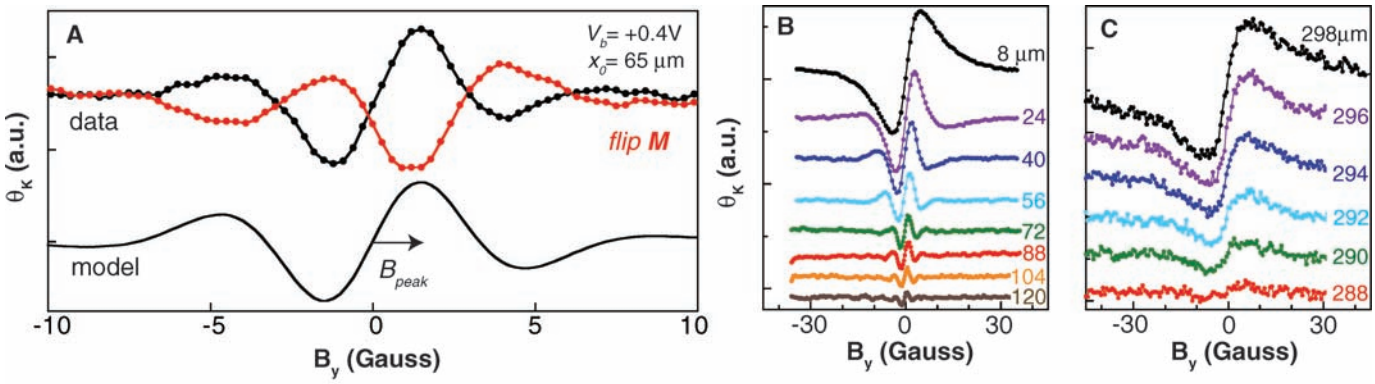

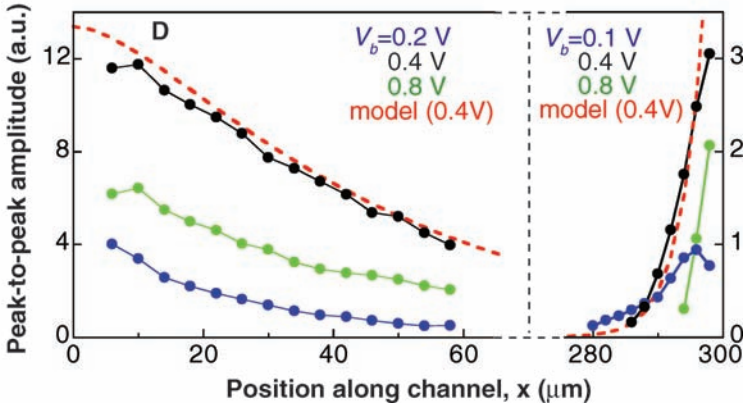

Fig. 3. (**A**) $\theta_K(B_y)$ curves due to injected spins, measured at x_0 = 65 μm from the source contact, for both directions of Fe magnetization **M**. The solid line is a model based on Eq. 1. (**B**) $\theta_K(B_y)$ data acquired at increasing distance from the source contact, showing electrical spin injection persisting out to 120 μm in the *n*-GaAs channel. V_b = +0.4 V. (**C**) Same as (B), but measured at 2-μm increments from the drain contact. (**D**) The peak-to-peak amplitude of the $\theta_K(B_y)$ curves versus distance from the source and drain contacts, for different biases $+V_b$. The dotted line shows the modeled amplitude from Eq. 1 using V_b = +0.4 V, τ_s = 125 ns, and v_d = 2.8 × 10^4 cm/s.

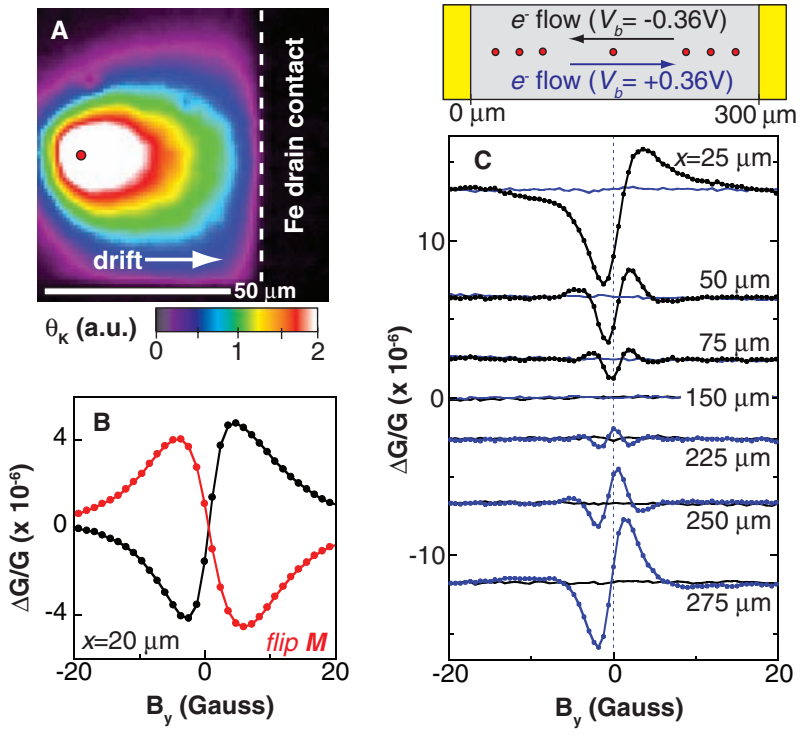

Fig. 4. (**A**) Image of θ_K, showing optically injected electrons, spin polarized along $+\hat{z}$, flowing into the drain contact (V_b = +0.36 V, B_y = 0). (**B**) Normalized conductance modulation $\Delta G/G$ versus B_y for both orientations of Fe magnetization **M**. The high-conductance state occurs when spins flowing through drain are polarized parallel to **M** and the low conductance state occurs when they are antiparallel. (**C**) $\Delta G/G$ versus B_y, for V_b = ±0.36 V, due to spin-polarized optical injection at the positions indicated.

The amplitudes of the $\theta_K(B_y)$ curves near the source and drain contacts are plotted in Fig. 3D for three bias voltages. The exponential decay length for injected spins increases with bias, from ~20 μm at V_b = 0.2 V to ~50 μm at V_b = 0.8 V, as electrons flow more quickly down the channel. In contrast, the accumulated spin polarization extends nearly one spin diffusion length (~10 μm) from the drain at low bias, but this length scale decreases to only a few μm at high bias, because polarized electrons can no longer diffuse backstream against the drift current (*25*). The dotted lines simulate the amplitude decay, using Eq. 1. Experimental $\theta_K(B_y)$ curves with increasing bias from 50 mV to 1.0 V are shown in fig. S3.

Finally, we show that the Fe/GaAs tunnel barriers also function as spin detectors. We optically inject spin-polarized electrons into the *n*-GaAs channel by using a weak laser beam (785 nm, 50 μW) focused to a 4-μm spot. Under bias, these polarized electrons flow into the drain contact (Fig. 4A). The laser polarization is modulated from right- to left-circular (injecting spins along $\pm\hat{z}$) at 50 kHz. The spins precess about B_y as they drift, arriving at the drain with some spin polarization parallel or antiparallel to **M**, depending on the injected spin orientation. We measure the corresponding modulation in the conductance, ΔG, as a function of B_y (*26*–*28*). The spin drift-diffusion equations apply equally well here, and the $\Delta G(B_y)$ curves (Fig. 4B) therefore resemble the $\theta_K(B_y)$ data discussed above. The high-conductance state occurs when the spins flowing through the drain contact are polarized parallel to **M**. This result is consistent with an accumulated (reflected) spin polarization that is antiparallel to **M**. In Fig. 4C, $\Delta G(B_y)$ is shown for both positive

(blue) and negative (black) bias at different injection positions along the channel. Both the amplitude and width of the curves decrease with increasing distance from the drain contact, similar to the previous $\theta_K(B_y)$ data. These data provide conclusive evidence that the Fe/GaAs Schottky tunnel barriers in lateral devices function as both spin detectors and injectors.

These measurements provide a detailed picture of spin transport in simple ferromagnet/semiconductor lateral structures. Smaller lateral dimensions and additional components, including a means to switch the source and drain contacts independently, will enhance the functionality of these devices. Although developing a purely electrical spin-transport device using a field effect or other means for spin manipulation remains a great challenge (*29*), the integration of an electrical injector and detector in a lateral structure represents an important step toward this goal.

References and Notes

1. A. T. Hanbicki *et al.*, *Appl. Phys. Lett.* **82**, 4092 (2003).
2. X. Jiang *et al.*, *Phys. Rev. Lett.* **94**, 056601 (2005).
3. C. Adelmann, X. Lou, J. Strand, C. J. Palmstrøm, P. A. Crowell, *Phys. Rev. B* **71**, 121301 (2005).
4. V. F. Motsnyi *et al.*, *Appl. Phys. Lett.* **81**, 265 (2002).
5. J. M. Kikkawa, D. D. Awschalom, *Nature* **397**, 139 (1999).
6. Y. Kato, R. C. Myers, A. C. Gossard, D. D. Awschalom, *Nature* **427**, 50 (2004).
7. S. A. Crooker, D. L. Smith, *Phys. Rev. Lett.* **94**, 236601 (2005).
8. Y. K. Kato, R. C. Myers, A. C. Gossard, D. D. Awschalom, *Phys. Rev. Lett.* **93**, 176601 (2004).
9. Y. K. Kato, R. C. Myers, A. C. Gossard, D. D. Awschalom, *Science* **306**, 1910 (2004).
10. J. Wunderlich, B. Kaestner, J. Sinova, T. Jungwirth, *Phys. Rev. Lett.* **94**, 047204 (2005).
11. M. Johnson, R. H. Silsbee, *Phys. Rev. Lett.* **55**, 1790 (1985).
12. F. J. Jedema, H. B. Heersche, A. T. Filip, J. J. A. Baselmans, B. J. van Wees, *Nature* **416**, 713 (2002).
13. P. R. Hammar, B. R. Bennett, M. J. Yang, M. Johnson, *Phys. Rev. Lett.* **83**, 203 (1999).
14. F. G. Monzon, H. X. Tang, M. L. Roukes, *Phys. Rev. Lett.* **84**, 5022 (2000).
15. B. J. Van Wees, *Phys. Rev. Lett.* **84**, 5023 (2000).
16. P. R. Hammar, M. Johnson, *Phys. Rev. Lett.* **88**, 066806 (2002).
17. Materials and methods are available as supporting material on *Science* Online.
18. J. Stephens *et al.*, *Phys. Rev. Lett.* **93**, 097602 (2004).
19. G. E. Pikus, A. N. Titkov, in *Optical Orientation*, F. Meier, B. P. Zakharchenya, Eds. (North-Holland, Amsterdam, 1984), pp. 73–131.
20. C. Ciuti, J. P. McGuire, L. J. Sham, *Phys. Rev. Lett.* **89**, 156601 (2002).
21. R. K. Kawakami *et al.*, *Science* **294**, 131 (2001).
22. R. J. Epstein *et al.*, *Phys. Rev. B* **65**, 121202R (2002).
23. The temporal integral in Eq. 1 is the one-dimensional, strain-free, Green's-function solution to the drift-diffusion equation.
24. Y. K. Kato, R. C. Myers, A. C. Gossard, D. D. Awschalom, *Appl. Phys. Lett.* **87**, 022503 (2005).
25. Z. G. Yu, M. E. Flatte, *Phys. Rev. B* **66**, 201202R (2002).
26. The absence of a ferromagnet in the injection region of these lateral devices and the detection of transverse spin at small magnetic fields avoid complications that have affected previous efforts to electrically detect optically oriented spins (*27*, *28*).
27. A. Hirohata, Y. B. Xu, C. M. Guertler, J. A. C. Bland, S. N. Holmes, *Phys. Rev. B* **63**, 104425 (2001).
28. A. F. Isakovic *et al.*, *J. Appl. Phys.* **91**, 7261 (2002).
29. S. Datta, B. Das, *Appl. Phys. Lett.* **56**, 665 (1990).

30. We thank L. Sham for valuable discussions and H.-J. Jang for technical assistance. This work was supported by the Defense Advanced Research Projects Agency's SpinS and Los Alamos Laboratory Directed Research and Development programs, the NSF Materials Research Science and Engineering Center program under grant DMR 02-12032, the Office of Naval Research, and the Minnesota Nanofabrication Center, which is supported by the NSF National Nanotechnology Infrastructure Network program.

Supporting Online Material

www.sciencemag.org/cgi/content/full/309/5744/2191/DC1
Materials and Methods
Figs. S1 to S3

1 July 2005; accepted 25 August 2005
10.1126/science.1116865

Embedded Nanostructures Revealed in Three Dimensions

I. Arslan,[1]* T. J. V. Yates,[1] N. D. Browning,[2,3] P. A. Midgley[1]

Nanotechnology creates a new challenge for materials characterization because device properties now depend on size and shape as much as they depend on the traditional parameters of structure and composition. Here we show that Z-contrast tomography in the scanning transmission electron microscope has been developed to determine the complete three-dimensional size and shape of embedded structures with a resolution of approximately 1 cubic nanometer. The results from a tin/silicon quantum dot system show that the positions of the quantum dots and their size, shape, structure, and formation mechanism can be determined directly. These methods are applicable to any system, providing a unique and versatile three-dimensional visualization tool.

The past decade has seen device technology enter the realm of nanoscale engineering for a large number of different applications. Many applications involve nanostructures that are embedded in other materials, where it is the size, shape, composition, and chemical interaction with the matrix that are key in determining the overall functionality of the device. Site-specific quantum-dot markers in live cells (*1*), inorganic nanostructures within self-assembled organic or biological templates (*2*), semiconductor nanocrystals (*3*) and metal tips grown on quantum rods and tetrapods (*4*), and catalytic growth of nanowires and nanostructures (*5*) are just some examples of new systems where the size, shape, and location (interaction) of the nanostructures are the critical parameters.

Transmission electron microscopy (TEM) and its variants have given us insight into nanoscale materials issues for over half a century. However, the vast majority of previous studies have made use of the periodicity of the sample (crystal structure) in the direction of the beam propagation, and they only involved the recording of a single two-dimensional (2D) projection (image) to understand the relationships between the structure and its properties. In nanostructures, the periodicity of the crystal structure in the beam direction does not continue indefinitely, and in fact, exactly when and how the periodicity terminates determines the material's properties. In such a case, a single 2D projection of the 3D object can at best give only partial information, and at worst be very misleading. Overcoming the ambiguity in the interpretation of a single 2D projection has been the driving force behind the very recent development of electron tomography that allows materials to be studied in 3D.

The conventional method to study structures with TEM is through high-resolution phase-contrast imaging (*6*, *7*). However, the relatively new technique of scanning transmission electron microscopy (STEM) can be superior to conventional TEM for some materials applications because of the incoherent nature of the imaging, the sensitivity to the atomic number Z of the species in the samples (Z-contrast imaging), direct interpretability, and the possibility of concurrent spectroscopy on the atomic scale (*8*–*12*). In general, electron tomography using Z-contrast imaging in a STEM is the most useful way to study crystalline inorganic nanomaterials in 3D. The reason is that diffraction contrast, which is seen in many bright-field and dark-field TEM images, violates the projection requirement, which states that the signal used for tomographic reconstructions must be a monotonic function of a physical property (*13*). The projection requirement must be fulfilled for a successful 3D reconstruction of the object from the series of 2D tilt images.

We used STEM tomography to study tin-rich (Sn) quantum dots embedded in a silicon

[1]Department of Materials Science and Metallurgy, University of Cambridge, Pembroke Street, Cambridge, CB2 3QZ, UK. [2]Department of Chemical Engineering and Materials Science, University of California, One Shields Avenue, Davis, CA 95616, USA. [3]National Center for Electron Microscopy, Lawrence Berkeley National Laboratory, One Cyclotron Road, Berkeley, CA 94720, USA.

*To whom correspondence should be addressed. E-mail: ia250@cam.ac.uk